Zhen Cao
Levent Yobas

Department of Electronic and Computer Engineering, Hong Kong University of Science and Technology, Kowloon, Hong Kong

Received February 26, 2014
Revised April 28, 2014
Accepted May 28, 2014

Research Article

Induced hydraulic pumping via integrated submicrometer cylindrical glass capillaries

Here, we report on a micropump that generates hydraulic pressure owing to a mismatch in EOF rates of microchannels and submicrometer cylindrical glass capillaries integrated on silicon. The electrical conductance of such capillaries in the dilute limit departs from bulk linear behavior as well as from the surface-charge-governed saturation in nanoslits that is well described by the assumption of a constant surface charge density. The capillaries show rather a gradual decrease in conduction at low salt concentrations, which can be explained more aptly by a variable surface charge density that accounts for chemical equilibrium of the surface. The micropump uses a traditional cross-junction structure with ten identical capillaries integrated in parallel on a side arm and each with a 750 nm diameter and 3 mm length. For an applied voltage of 700 V, a hydraulic pressure up to 5 kPa is generated with a corresponding flow velocity nearly 3 mm/s in a straight field-free branch 20 μm wide, 10 μm deep, and 10 mm long. The micropump utility has been demonstrated in an open tubular LC of three fluorescently labeled amino acids in just less than 20 s with minimal plate height values between 3 and 7 μm. The submicrometer capillaries are self-enclosed and produced through a unique process that does not require high-resolution advanced lithography or wafer-bonding techniques to define their highly controlled precise structures.

Keywords:
Capillary / Chromatography / Microfluidics / Micropump / Surface charge
DOI 10.1002/elps.201400099

1 Introduction

1.1 General aspects

Precise control of nL to fL liquid manipulation through microscopic channels and capillaries without relying on complicated hardware poses a great technological barrier against the practical applications of lab on a chip and microfluidic devices [1,2]. To address this challenge, numerous miniaturized pumps and valves with various actuation principles have been demonstrated and also further discussed in comprehensive reviews on the topic [3, 4]. Of those, mechanical types face complex microfluidic integration and the associated reliability issues [5, 6].

Electrokinetic control of flow, in particular EOF is arguably the most convenient, as it involves neither moving parts nor leak-proof tubing interfaces to an external pressure or vacuum source [7–9]. EOF originates from diffused counter-ions within electrical double layer (EDL) that drift under a tangentially applied field and drag along the liquid layers in a nearly uniform plug flow. EDL spontaneously builds up near the channel boundaries, charged upon in contact with a polar liquid, and translates the applied time-invariant field to a nonpulsating EOF with rate and direction determined by the field magnitude and polarity. Thus, EOF can be accurately and rapidly switched by simply modulating the field. The utility of EOF in micro/nanofluidics, apart from pumping [10], is numerous from chemical separations [7] to liquid injection or dispensing [11], and from analyte enrichment [12,13] to mixing [14,15]. Nevertheless, EOF rates are sensitive to surface properties, which may undesirably vary with the pH of the background solution as well as with irreversible adsorption of the charged analytes [16,17]. In return, reproducibility and reliability suffer. Moreover, applications such as chromatographic separation, require, a pressure-driven flow, despite the poor control dynamics due to large dead volume in fluidic interfacing, so as not to instigate electrophoretic disturbances on those analytes interacting with the stationary phase [18,19].

The notion of inducing hydraulic pumping through EOF is highly attractive as it helps decouple such disturbances by keeping the analytes in a field-free region while leveraging on the benefits of EOF control without the articulated drawbacks [20,21]. Hydraulic pressure gradient stems from a

---

Correspondence: Dr. Levent Yobas, Department of Electronic and Computer Engineering, Hong Kong University of Science and Technology, Clear Water Bay, Kowloon, Hong Kong
E-mail: eelyobas@ust.hk
Fax: +85-22-358-1485

Abbreviations: DRIE, deep reactive ion etching; **EDL**, electrical double layer; **ODS**, octadecyltrichlorosilane

Colour Online: See the article online to view Figs. 1, 2, 4–6 in colour.

designed mismatch in EOF rates between the branches of a node such that the mass is conserved (incompressible flow) [21–23]. Strategies to introduce such deliberate mismatch in EOF rates predominantly involve modulating the surface potential (ζ) through selective surface coatings [21, 23] or more dynamically through surface-embedded electrodes [20, 24] or simply through buffers of varying ionic strengths [22].

Ramsey and Ramsey applied a viscous polymer (polyacrylamide) surface coating to suppress the local EOF of a select branch and utilized the induced pressure to drive an on-chip electrospray [21]. Culbertson et al. subsequently applied this concept to selectively transport anions down to a field-free branch [23]. Dutta and Ramsey replaced polyacrylamide with a polyelectrolyte multilayer, altering the surface charge polarity and the direction of EOF instead of suppressing it [25]. The authors then performed a pressure-driven separation in a field-free branch. McKnight et al., by setting local potentials inside a straight microchannel through thin-film contact electrodes, exclusively applied the field across the desired channel segment [24]. Sniadecki et al. dynamically modulated ζ potentials through field effect by surface-embedded electrodes [20]. Razunguzwa and Timperman packed anion and cation exchange beads in branches converging into a field-free outlet and demonstrated a pump with a reduced pH dependence [26]. Joo et al. substituted the beads with a polyelectrolyte surface coating having an appropriate polarity and utilized the induced pressure for gated field-free injection and particle sorting [27]. Chien and Bousse introduced a nonuniform electric flux and a subsequent induced hydraulic pressure through electrolytes with distinct ionic conductivities [22].

Recently, an alternative way of introducing the required mismatch in EOF rates has been demonstrated based on a striking discovery on the aqueous-filled slits as thin as 70 nm [28–30]. Stein et al. found that the electrical conductance through such slits saturates at a level independent of both the slit depth and salt concentration in the dilute limit below a transition concentration reportedly higher for shallower slits [28]. This is attributed to the electrostatic effects of the slit surface charge on the low-salt ionic transport and occurs under conditions far from the regime of local electrical double layer overlap [28, 29]. Yanagisawa and Dutta used this principle to induce a differential electric flux at a node with a branch segment deliberately made shallower (≤3 μm) [30]. For an applied potential of 1.7 kV, the authors reported pressure driven velocities up to 3.2 mm/s in a field-free branch and a corresponding maximum pressure 6.3 kPa that was shown to operate a reverse-phase chromatographic separation with minimal plate height. This appealing method is rather immune to the issues concerning stability, repeatability, lifetime, and electrolytic bubbles.

Here, using the same principle, we demonstrate hydraulic pumping in a novel silicon device whereby slits are replaced with cylindrical glass capillaries. We find that such capillaries, owing to higher order confinement, deviate notably from slits in low-salt ionic transport. First and foremost, the apparent conductivity through such conduits begins to diverge from bulk conductivity at a higher salt ionic concentration, which exceeds that of slits by about two orders of magnitude. Second, the transition concentration, where the conductance begins to plateau, is nearly three orders of magnitude lower in capillaries than slits. In return, per applied voltage, capillaries yield about twice as high hydraulic pressure and flow rate as slits do. The cylindrical glass capillaries shown here are less than 1 μm in diameter and fabricated through thermal reflow of doped glass layer in trenches patterned on silicon by a coarse photolithography (≥2 μm) [31, 32]. The device utility is demonstrated through an open-tubular liquid chromatographic separation of amino acids with minimal plate heights. Dielectrophoresis, the motion of a polarizable analyte due to the action of the nonuniform electric field at the junction of the capillaries and microchannel, is not considered. The dielectrophoretic forces, although they are present under constant applied fields, are localized at the junction and scale with the volume of the analyte [33]. The nanometer-sized analytes (e.g. amino acids) might experience such forces but only briefly before entering into the field-free branch and typically in the femtonewton range, insignificant in comparison to the convective forces due to electrosmosis and induced pressure [34–36].

2 Materials and methods

2.1 Device design and fabrication

Figure 1 schematically describes the device design and the cylindrical glass capillary fabrication. The device integrates a cross-junction structure for sample injection and a straight microchannel, which is 10 mm long and 20 μm wide, for field-free separation. In a side arm, the cross-junction structure contains a parallel arrangement of 10 such capillaries 750 nm in diameter and 3 mm in length. Apart from the capillaries, all the channels are of a rectangular profile 10 μm deep. The cylindrical capillaries are built through reflow of an annealed glass layer in rectangular trenches about 3 μm wide and 3.5 μm deep. As described in Fig. 1B, nonconformal deposition of a thick glass layer traps an elongated void within a trench as a result of pinching and sealing off the trench opening before the trench gets entirely filled up. This phenomenon is well known from the fabrication of integrated circuits where it leads to device complications and hence undesired. Although the voids are of a triangular shape, they undergo shape transformation through thermal reflow of glass and turn into buried cylindrical capillaries in trenches so as to minimize their free surface energy. Previously, we demonstrated such capillaries in various lengths and diameters for applications concerning patch-clamp electrophysiology of individual cells [37–39], electrophoretic separation of amino acids [40], stretching of DNA molecules under physical confinement [41], and rapid sieving of large DNA molecules in free solution [42]. Since these capillaries are self-enclosed and entirely buried in trenches, defining their fluidic access ports can be a challenge due to the requirement of dry

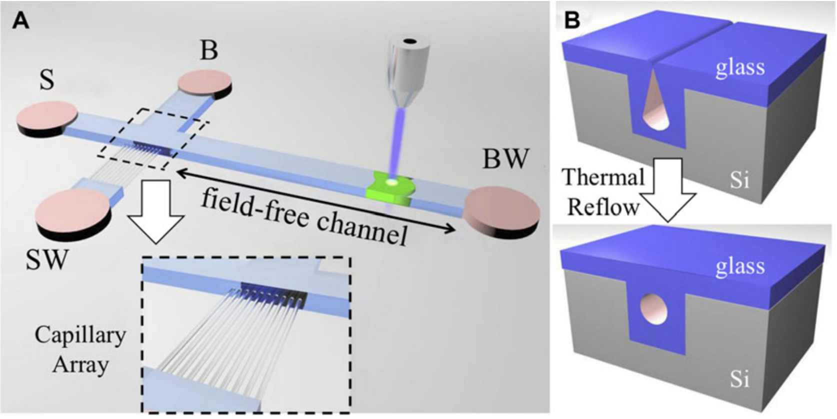

Figure 1. 3D rendering of (A) the overall design and (B) the cylindrical glass capillary integration. (A) The cross-junction design involves an integrated capillary array (inset) in one arm and allows a sample plug to be electrokinetically introduced and pressure driven down the field-free analysis channel where it gets chromatographically separated and detected. (B) An elongated void being trapped in a trench partially filled with a doped glass layer due to nonconformal deposition (upper panel) and the void upon shape transformation through glass thermal reflow (lower panel).

etching glass. We resolved this issue by having both trench ends open up to deeper channels as they gradually expand in width. This approach naturally forms the access ports along with the capillaries upon thermal reflow of glass [40,42].

The device was fabricated using the same process steps as those we recently reported for a different layout, capillary-well array, and for the rapid sieving of long DNA chains in free solution [42]. A dual-step profile was imparted on silicon by deep reactive ion etching (DRIE) initially through a photoresist mask (to form the reservoirs/channels 10 μm deep) and then, upon stripping off the resist mask, through a silicon dioxide mask (to form the trenches 3 μm wide and 3.5 μm deep). The two masks were prepared on the substrate prior to the DRIE steps. The structured substrates were then passivated with a 0.7-μm thermal oxide underneath a nonconformal layer of 5-μm thick phosphosilicate glass placed through a low-pressure chemical vapor deposition process (180 mTorr, 420°C). The triangular voids, the so-called capillary precursors, were transformed into cylindrical capillaries with the doped glass layer reflow in a thermal anneal step at 1000°C for 1 h. The device was individually aligned and permanently bonded with a plain slab of PDMS (Dow Corning 184) bored with four inlet/outlet ports upon activating their surfaces in oxygen plasma (29.6 W, 45 s, Harrick Plasma).

2.2 Operation procedure

Figure 2 outlines the gated injection of a sample plug into the field-free channel (segment C) under the induced hydraulic pressure. Each step is further described by a representative image (inset) captured using Rhodamine B neutral dye. The device was first filled with the DI water or sodium borate buffer (pH 9.2) of a chosen concentration directly dispensed into reservoirs S, SW, B, and BW (as labeled in Fig. 2). The sample was pipetted into reservoir S. The liquid levels in all the reservoirs were balanced before placing the platinum wire electrodes (Leego Precision Alloy, China). No electrode was placed in reservoir BW to keep segment C field free. Throughout the procedure, reservoir SW was kept at a ground potential while reservoirs S and B were set at equally high potentials (e.g. 500 V) to avoid sample leakage (Fig. 2A). For gated injection, reservoir B was momentarily switched to ground (for ~2 s) to have a plug of sample proceed into the field-free channel (Fig. 2B). Immediately after, both reservoirs B and S were stepped to a test potential releasing the sample plug under the induced hydraulic pressure into the field-free channel (Fig. 2C). The sample plug was detected 1 cm downstream of the injection cross by fluorescence emission of Rhodamine B or FITC. Based on the measured travel time, the pressure-driven flow velocities were calculated for the respective test potentials. Subsequently, the induced hydraulic pressure values were inferred from the estimated fluidic resistance values of the channels.

2.3 Instruments

The device under test was observed through an epi-fluorescence microscope (FN1; Nikon, Japan) equipped with a mercury lamp (100 W) and a filter cube set for fluorescence detection (FITC: Ex/Em 492/520 nm; Rhodamine B: Ex/Em 540/625 nm). Images were captured to a computer via a 10× objective and a CCD camera (RT3 Mono; SPOT) mounted on the microscope. The prescribed electrical potentials were delivered from a multi-channel high-voltage power supply (Tianjin Dongwen Co., China) controlled by LABVIEW (National Instruments).

2.4 Liquid chromatography

The stationary phase was prepared by selectively coating the field-free channel (segment C) through a procedure adopted after Kohr and Engelhardt [43]. The channels were successively rinsed with 1 M sodium hydroxide solution (10 min), DI water (5 min), and 1 M hydrochloric acid (10 min) before a final rinse in DI water (5 min) and a subsequent overnight incubation at 120°C. Afterwards, all the reservoirs but BW were filled with dry toluene whereas reservoir BW was filled with 1% w/w octadecyltrichlorosilane (ODS) freshly prepared in dry toluene. By applying vacuum at reservoir B

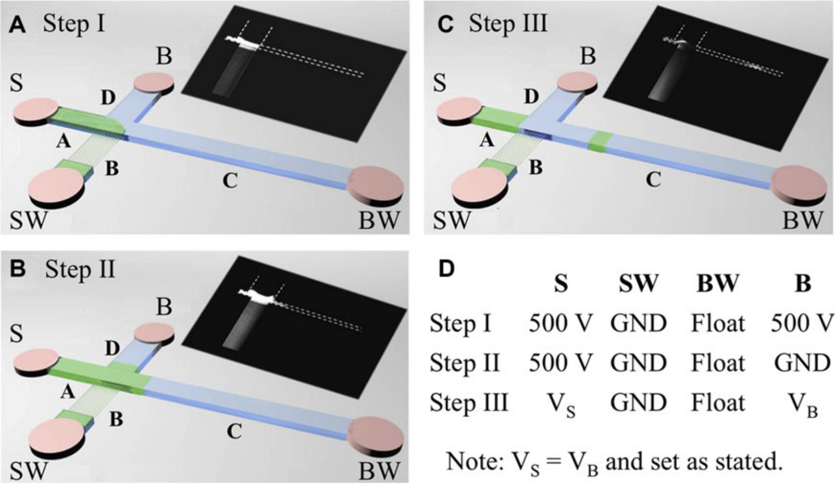

	S	SW	BW	B
Step I	500 V	GND	Float	500 V
Step II	500 V	GND	Float	GND
Step III	V_S	GND	Float	V_B

Note: $V_S = V_B$ and set as stated.

Figure 2. Electrokinetic-gated injection and hydraulic pressure-driven separation in the device as schematically described in sequential steps: (A) sample loading, (B) injection, and (C) separation. The insets are the fluorescence images from the device using Rhodamine B neutral dye as the sample analyte for illustration. (D) The voltage protocol accompanying each step as listed. Note that no electrode was placed in reservoir BW to leave segment C field free.

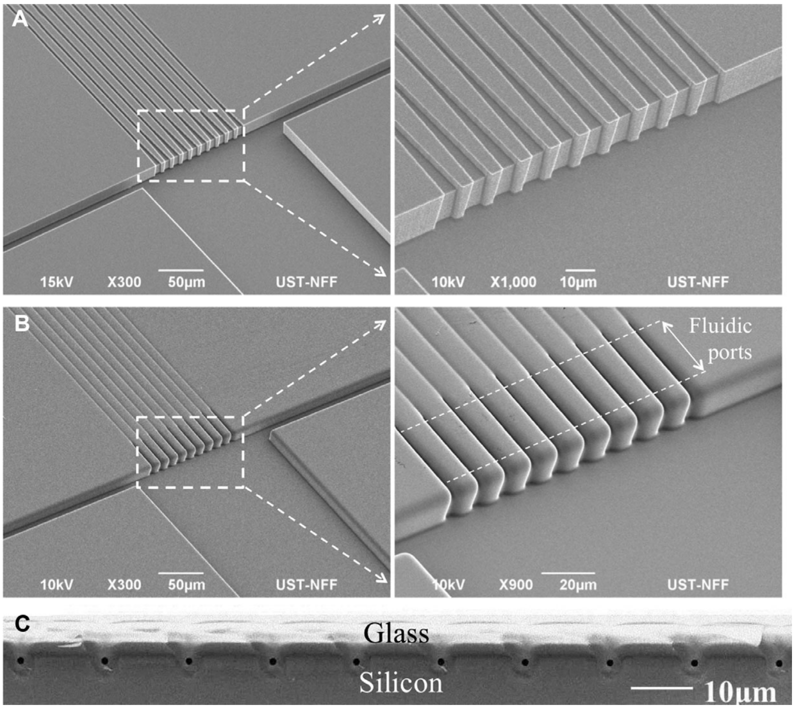

Figure 3. SEM images of a representative device cross-junction before (A) and (B) after a doped glass layer deposition and subsequent thermal reflow. The dashed rectangles highlight the regions enlarged in the adjacent images to depict gradually expanding trench widths and the resultant self-formed fluidic access ports between the dashed lines. (C) Cross-sectional view of the capillary array away from the access ports (ten highly ordered capillaries, each 750 nm in diameter).

for 10 min, the field-free channel was selectively coated with ODS as being the stationary phase. The unreacted silanol groups were then removed with dry toluene. During the procedure, the device was placed in a container with a saturated toluene atmosphere to prevent reservoirs from drying. FITC-labeled aspartic acid, glycine, and phenylalanine were prepared and diluted to a concentration of 0.1 mM in mobile phase, containing 30% w/w acetonitrile in 1 mM sodium borate buffer. The sample was then pipetted in reservoir S and the steps described above were applied for gated-injection of the sample plug and the subsequent separation of the FITC-labeled amino acids in the field-free channel coated with the solid phase. Time-series fluorescent images were recorded from a detection point 1 cm downstream of the injection cross and then analyzed offline by an image processing software (ImageJ; NIH, Bethesda) to generate chromatograms by extracting and plotting fluorescence intensities from region of interest (ROI ~ 20 μm by 20 μm). Peaks were analyzed and fitted to Gaussians using software Matlab (Mathworks).

3 Results and discussion

3.1 Capillaries

Figure 3 depicts the sample-injection junction before and after deposition/reflow of doped glass. The junction adopts a dual-step profile where the individual trenches can be seen gradually expanding from a nominal width of 3 μm and terminating at a width of 7 μm. This diverging section is about 50 μm long and leads to funnel-like access ports with a characteristic appearance (between the dashed lines, Fig. 3B). Sectioning the capillaries away from the access ports further reveals their cross-sectional profile, which was found to be highly uniform remarkably consistent in diameter, which is 750 nm (Fig. 3C). To accommodate the capillaries and their interspacing, the side arms are designed to be 200 μm wide. This width could be further scaled down by more densely packing the capillaries.

3.2 Capillary conductance

Figure 4 shows the characteristic dc conductance through the ten parallel glass capillaries integrated in the device as a function of the salt concentration varied over six orders of magnitude. For comparison, the dc conductance curve reported by Stein et al. based on a silica nanoslit is also shown [28]. The nanoslit is 70 nm deep, 50 μm wide, and 4.5 mm long, comparable to the capillary array here in total volume, 15.8 vs. 13.3 pL, and cross-sectional area, 3.5 vs. 4.4 μm^2, but with a larger surface area, 0.45 vs. 0.07 mm^2, respectively. The dashed (blue) line shown represents the expected conductance linear behavior for both the capillaries as well as the slit based on the measured bulk conductivity and geometrical dimensions under the assumption of surface neutrality. As can be seen, the conductance measured through the capillaries begins to diverge from the expected linear trend at a higher salt concentration (>0.1 M KCl) while the slit conductance stays with the linear trend down to 10 mM where it saturates. Strikingly, the capillaries saturate at a lower salt ionic concentration (10 μM) when they are about to exceed the expected conductance level by 2–3 orders of magnitude.

Stein et al. attribute the saturation observed with the low-salt ionic transport in a nanoslit to the electrostatic effects of the slit surface charge exerted on the fluid [28]. At high salt concentrations, the charge carriers in the bulk solution (K$^+$ and Cl$^-$) dominate the ionic conduction. Hence bulk behavior is observed and the conductance scales linearly with the concentration. However, with the reduced salt concentration, bulk ions are surpassed by the excess mobile K$^+$ counterions gathered to neutralize negative surface charge of the silica nanoslit while Cl$^-$ coions get repelled. The conductance is then governed by the excess counterions responsible for the limiting behavior. At any concentration, the conductance through the slit or capillary can be therefore modeled as the algebraic sum of the terms arising from bulk ions and the counterions [29, 44]:

$$G_{s,c} = \frac{A_{s,c}}{l_{s,c}}\left[(\mu_K + \mu_{Cl})\, c\, N_A e + \mu_K \frac{2\sigma^*_{s,c}}{d_{s,c}}\right] \qquad (1)$$

where $A_{s,c}$ and $l_{s,c}$ are the cross-sectional area and the length of the slit or capillary, respectively, $d_{s,c}$ is the slit height or the capillary radius, μ_K and μ_{Cl} are the electrophoretic mobility values of the potassium and chloride ions, respectively, ($\mu_K = 7.62 \times 10^{-8}$ m^2/Vs and $\mu_{Cl} = 7.91 \times 10^{-8}$ m^2/Vs), c is the bulk concentration of ions, N_A is Avogadro's number, e is the electron charge, and $\sigma^*_{s,c}$ is the effective surface charge density on the slit or the capillary.

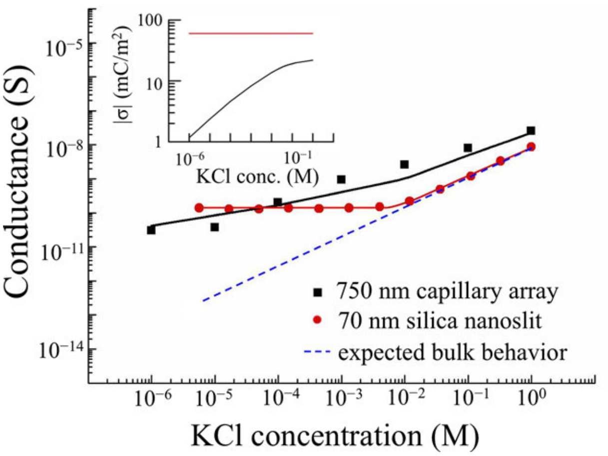

Figure 4. Plot of conductance as a function of KCl concentration from 1 μM to 1 M showing the experimentally measured values from the capillary array on the device (squares) in comparison to those from the silica nanoslit as reported by Stein et al. (circles) [28]. The capillaries (ten of them in parallel) are all identical each 750 nm in diameter and 3 mm in length while the reported nanoslit is 70 nm in height, 50 μm in width and 4.5 mm in length. The dashed (blue) line depicts the expected conductance values from the either device based on the conductivity of bulk KCl. The fitting lines are obtained from Eq. (1) using either a constant surface charge ($\sigma^*_{s,c} = 60$ mC/m^2) for the nanoslit (red) or a variable surface charge for the capillary array (black) given in the inset as a plot of the salt concentration vs. the absolute surface charge density in log-log scale.

For the nanoslit, Eq. (1) fits well to the experimental data based on a constant surface charge density of $\sigma^*_{s,c} = 60$ mC/m^2. However, it fails to describe the capillary conductance in the low-salt regime. Smeets et al. noticing a similar discrepancy in nanopores (diameter 10 nm) argued that the surface charge density should vary with the ion concentration to reflect the chemical reactivity of the silica surface SiOH groups [44]. To incorporate the chemical nature of the silica surface, the authors adopted a model developed by Van der Heyden et al. [45] and obtained a variable surface charge density function that fits reasonably well to their data according to Eq. (1). Applying their method to the capillaries here, we calculated and found a similar variable charge density (Fig. 4, inset) at a reasonable agreement with our data.

3.3 Induced hydraulic pressure

The induced hydraulic pressure in the device due to higher electrical conductance through the capillaries in the dilute limit and the resultant mismatch in EOF rates was experimentally evaluated by measuring the flow velocity in the separation channel (segment C). It should be emphasized that,

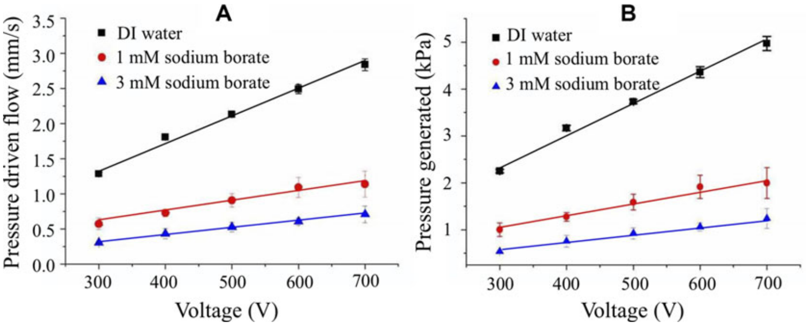

Figure 5. (A) Pressure-driven flow velocity measured in the field-free channel for various aqueous concentrations (inset) as a function of the voltage magnitude applied at reservoirs S and B and (B) the respective hydraulic pressure calculated from the estimated hydrodynamic resistance based on the channel geometries. The symbols and error bars represent mean ± SD ($n = 5$).

the separation channel, with no voltage applied across, remained entirely free of electric field. Thus, the observed flow was due to the induced hydraulic pressure. To observe the flow, a sample plug of neutral fluorescent dye (Rhodamine B) was introduced into the separation channel through the gated injection scheme as described earlier. Measuring the total travel time of the fluorescent plug through the 1 cm long channel provided a reasonable estimate of the average flow velocity. Fig. 5A shows a plot of the obtained values as a function of the voltage magnitude (applied at both reservoirs S and B) and the ionic strength of the BGE (deionized water or sodium borate buffer at 1 or 3 mM). Figure 5B also shows the corresponding values of the induced hydraulic pressure predicted based on the hydrodynamic resistance of the rectangular separation channel, $12\eta l/[wd^3(1 - 0.63d/w)]$, where l is the channel length, w is the width, d is the height, and η is the fluid viscosity (10^{-3} Pa s). The pressure-driven flow velocity, since it originates from EOF, was observed to increase inversely with the electrolyte ionic strength and linearly with the applied voltage magnitude. Thus, the highest flow velocity and induced hydraulic pressure were attained with DI water and at a maximum applied voltage of 700 V, corresponding to 2.84 mm/s and 4.9 kPa with a return of 4.06 μm s^{-1} V^{-1} and 7.1 Pa V^{-1}. In comparison, Yanagisawa and Dutta using DI water reported 3.2 mm/s and 6.3 kPa at 1.75 kV (1.83 μm s^{-1} V^{-1} and 3.6 Pa V^{-1}) in a field-free channel 15 μm deep, 150 μm wide, and 3.7 mm long [30]. The authors had a silica slit about 2 μm deep, 150 μm wide, and 2 mm long in a side arm of a cross-junction design. Although the reported values slightly exceed those here, they were obtained with much higher voltage. A further advantage of the capillaries is that their diameter can be scaled down through an extended anneal and without high-density lithography [41].

3.4 Open-tubular LC

The utility of the induced hydraulic pressure was demonstrated by performing open-tubular LC of three FITC-labeled amino acids in the field-free channel (segment C). The channel was selectively coated with a mixture of 1% ODS by weight in dry toluene as the stationary phase through a procedure detailed in Section 2. The mobile phase contained 30% acetonitrile by weight in a 1 mM sodium borate buffer. An aliquot of 100 μM amino acid mixture in the mobile phase was loaded in reservoir S and a sample plug was introduced into the separation channel under the hydraulic pressure induced by an applied voltage between 300 and 700 V. Figure 6A shows a representative chromatogram obtained at a detection point 1 cm downstream of the injection cross. As can be seen, the three amino acids were fully resolved in just under 20 s with the voltage at 500 V. Peaks were identified by the elution times of amino acids from independent injection of amino acid types and found consistent with the amino acid polarity. The number of theoretical plates (N) for the 1 cm channel, using phenylalanine as the reference peak, is 3764, equivalent to a plate height (H) of 2.7 μm. These values are either comparable or better than the reported open-tubular LC chips driven by an integrated pump. For instance, Dutta and Ramsey reported a plate height of about 8 μm for a 2 cm separation channel supplied by a junction with one arm selectively coated with a positively charged polyelectrolyte multilayer to introduce the required mismatch in EOF rates [25]. Fuentes and Woolley reported a plate height of 7.5 μm for a 2.5 cm separation channel integrated with an electrolysis-based pump [46]. The higher efficiency achieved here may result from a small injection volume (~10 pL).

A van Deemter plot revealing the measured reduced plate height (h) as a function of the reduced linear velocity of the mobile phase (v) is presented in Fig. 6B. The lowest reduced plate height values were in the range of 0.16–0.38 (H ~3–7 μm) and observed at a reduced linear velocity of the mobile phase from 12 to 22 (u ~0.7–1 mm/s). The curves were obtained by fitting the data to a generalized Knox equation:

$$h = Av^n + B/v + C_s v \tag{2}$$

where A, B, C, and n are constants. The A, B, and C terms represent eddy diffusion, longitudinal diffusion, and resistance to mass transfer, respectively. The exponent n is a variable chosen here to obtain the best fit. Table 1 lists the values that offered the best fits (R^2 values greater than 0.94) to the experimental data using the generalized Knox equation in nonlinear regression analysis. The reduced forms are given as:

$$h = H/w \tag{3}$$

$$v = uw/D_m \tag{4}$$

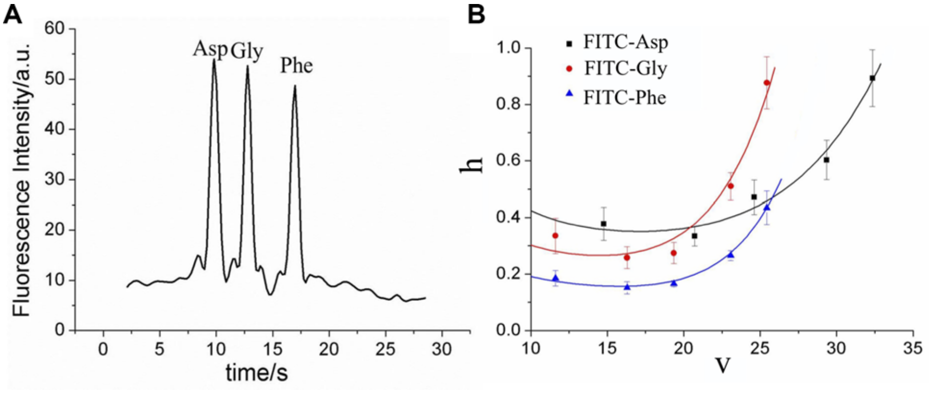

Figure 6. (A) Open channel liquid chromatography of FITC-labeled three amino acids under pressure-driven flow conditions in the device at 500 V. The chromatogram was obtained 1 cm from the injection cross and at a mobile phase velocity of 1 mm/s; (B) Reduced van Deemter experimental plots and the respective fitted curves according to the generalized Knox equation (Eq. (2)) with the parameter values as listed in Table 1. The symbols and error bars represent mean ± SD ($n = 5$).

Table 1. The Knox parameter values (Eq. (2)) that returned the best fits to the data (Fig. 6B)

Peak	$10^{11} A$	B	$10^3 C$	n
FITC-Asp	17.5	3.42	8.29	6.27
FITC-Gly	4.44	2.39	6.27	7.20
FITC-Phe	0.19	1.60	3.08	7.97

Asp, aspartic acid; Gly, glycine; Phe, phenylalanine.

where H and u are the plate height and the linear mobile phase velocity, respectively, w is the channel width 20 μm and D_m is the axial diffusion coefficients of amino acids, respectively, 8.3×10^{-6}, 10.55×10^{-6}, and 7.05×10^{-6} for aspartic acid, glycine and phenylalanine, all in cm^2/s [47].

For $n = 0$, Eq. (2) is simplified to the van Deemter equation. The van Deemter equation, however, returned a poor fit to the data for the nonnegative values of A, which implied peak compression and had no physical basis. Ideally, a zero A value was sought for signifying the lack of eddy diffusions in a straight open channel. The encounter of a negative A value has been recently reported and discussed by Sukas et al. for which the authors concluded that forcing the A term to be independent of the linear velocity is an oversimplification that leads to the loss of data [48].

4 Concluding remarks

We have demonstrated a micropump that can supply electrically induced hydraulic pressure by tapping on differential electrical conduction through the submicrometer glass capillaries at low salt concentrations. We have also measured the capillary array conductance and found that, as in the slits, it departs from the bulk linear behavior but unlike the slits gradually decreases with the salt concentration before it saturates. We have confirmed that the behavior is better described by a variable surface charge that accounts for the glass surface chemical equilibrium. We have measured the micropump characteristics in a field-free microchannel and observed pressure-driven flow velocities up to 3 mm/s, denoting a hydraulic pressure of 5 kPa, induced at 700 V. These rates, although they have been shown to scale linearly with the applied voltage and inversely with the salt concentration, have been found adequate to drive open-tubular LC of three amino acids to a complete separation in less than 20 s with a reasonable efficiency (plate heights: 3–7 μm).

Lastly, the micropump presented here can be further optimized in critical dimensions. The capillaries down to tens of nanometers in diameter are still within the realm of standard photolithography and can be obtained by tuning the aspect ratio of the trenches and thermal reflow conditions. Shorter capillaries and/or increased number of capillaries in parallel would increase the field share of the microchannels and their prospective EOF rates for an applied voltage, thereby enhancing the micropump capacity. As the pumping mechanism does not rely on a post-process treatment of a select surface region, the micropump demonstrated here is compact and convenient and may find use in other bioanalytical applications.

This work was supported by the Research Grant Council of Hong Kong under Grant 621513.

The authors have declared no conflict of interest.

5 References

[1] Whitesides, G. M., *Nature* 2006, *442*, 368–373.

[2] Squires, T. M., Quake, S. R., *Rev. Mod. Phys.* 2005, *77*, 977–1026.

[3] Laser, D. J., Santiago, J. G., *J. Micromech. Microeng.* 2004, *14*, R35–R64.

[4] Wang, X. Y., Cheng, C., Wang, S. L., Liu, S. R., *Microfluid. Nanofluid.* 2009, *6*, 145–162.

[5] Vanlintel, H. T. G., Vandepol, F. C. M., Bouwstra, S., *Sensor. Actuator.* 1988, *15*, 153–167.

[6] Yobas, L., Tang, K. C., Yong, S. E., Ong, E. K. Z., *Lab. Chip.* 2008, *8*, 660–662.

[7] Harrison, D. J., Fluri, K., Seiler, K., Fan, Z. H., Effenhauser, C. S., Manz, A., *Science* 1993, *261*, 895–897.

[8] Harrison, D. J., Manz, A., Fan, Z. H., Ludi, H., Widmer, H. M., *Anal. Chem.* 1992, *64*, 1926–1932.

[9] Seiler, K., Fan, Z. H. H., Fluri, K., Harrison, D. J., *Anal. Chem.* 1994, *66*, 3485–3491.

[10] Cao, Z., Yuan, L., Liu, Y. F., Yao, S., Yobas, L., *Microfluid. Nanofluid.* 2012, *13*, 279–288.

[11] Martin, M., Guiochon, G., *Anal. Chem.* 1984, *56*, 614–620.

[12] Nielen, M. W. F., *Trac-Trend. Anal. Chem.* 1993, *12*, 345–356.

[13] Cao, Z., Yobas, L., *Electrophoresis* 2013, *34*, 1991–1997.

[14] Glasgow, I., Batton, J., Aubry, N., *Lab. Chip.* 2004, *4*, 558–562.

[15] Chang, C. C., Yang, R. J., *Microfluid. Nanofluid.* 2007, *3*, 501–525.

[16] Li, Y., Xiang, R., Wilkins, J. A., Honrath, C., *Electrophoresis* 2004, *25*, 2242–2256.

[17] Revermann, T., Gotz, S., Kunnemeyer, J., Karst, U., *Analyst* 2008, *133*, 167–174.

[18] Kutter, J. P., *J. Chromatogr. A* 2012, *1221*, 72–82.

[19] Faure, K., *Electrophoresis* 2010, *31*, 2499–2511.

[20] Sniadecki, N. J., Lee, C. S., Sivanesan, P., DeVoe, D. L., *Anal. Chem.* 2004, *76*, 1942–1947.

[21] Ramsey, R. S., Ramsey, J. M., *Anal. Chem.* 1997, *69*, 2617–2617.

[22] Chien, F. L., Bousse, L., *Electrophoresis* 2002, *23*, 1862–1869.

[23] Culbertson, C. T., Ramsey, R. S., Ramsey, J. M., *Anal. Chem.* 2000, *72*, 2285–2291.

[24] McKnight, T. E., Culbertson, C. T., Jacobson, S. C., Ramsey, J. M., *Anal. Chem.* 2001, *73*, 4045–4049.

[25] Dutta, D., Ramsey, J. M., *Lab. Chip.* 2011, *11*, 3081–3088.

[26] Razunguzwa, T. T., Timperman, A. T., *Anal. Chem.* 2004, *76*, 1336–1341.

[27] Joo, S., Chung, T. D., Kim, H. C., *Sensor. Actuat. B-Chem.* 2007, *123*, 1161–1168.

[28] Stein, D., Kruithof, M., Dekker, C., *Phys. Rev. Lett.* 2004, *93*, 035901.

[29] Schoch, R. B., Renaud, P., *Appl. Phys. Lett.* 2005, *86*, 253111.

[30] Yanagisawa, N., Dutta, D., *Electrophoresis* 2010, *31*, 2080–2088.

[31] Agarwal, A., Ranganathan, N., Ong, W. L., Tang, K. C., Yobas, L., *Sensor. Actuat. A Phys.* 2008, *142*, 80–87.

[32] Wong, C. C., Agarwal, A., Balasubramanian, N., Kwong, D. L., *Nanotechnology* 2007, *18*, 135304.

[33] Regtmeier, J., Eichhorn, R., Viefhues, M., Bogunovic, L., Anselmetti, D., *Electrophoresis* 2011, *32*, 2253–2273.

[34] Nakano, A., Ros, A., *Electrophoresis* 2013, *34*, 1085–1096.

[35] Hölzel, R., Calander, N., Chiragwandi, Z., Willander, M., Bier, F. F., *Phys. Rev. Lett.* 2005, *95*, 128102(1)–128102(4).

[36] Stein, D., Deurvorst, Z., van der Heyden, F. H. J., Koopmans, W. J. A., Gabel, A., Dekker, C., *Nano. Lett.* 2010, *10*, 765–772.

[37] Tang, K. C., Reboud, J., Kwok, Y. L., Peng, S. L., Yobas, L., *Lab. Chip.* 2010, *10*, 1044–1050.

[38] Ong, W. L., Kee, J. S., Ajay, A., Ranganathan, N., Tang, K. C., Yobas, L., *Appl. Phys. Lett.* 2006, *89*, 093902.

[39] Ong, W. L., Tang, K. C., Agarwal, A., Nagarajan, R., Luo, L. W., Yobas, L., *Lab. Chip.* 2007, *7*, 1357–1366.

[40] Cao, Z., Ren, K. N., Wu, H. K., Yobas, L., *Biomicrofluidics* 2012, *6*, 036501.

[41] Liu, Y. F., Yobas, L., *Biomicrofluidics* 2012, *6*, 046502.

[42] Cao, Z., Yobas, L., *Anal. Chem.* 2014, *86*, 737–743.

[43] Kohr, J., Engelhardt, H., *J. Chromatogr. A* 1993, *652*, 309–316.

[44] Smeets, R. M. M., Keyser, U. F., Krapf, D., Wu, M. Y., Dekker, N. H., Dekker, C., *Nano Lett.* 2006, *6*, 89–95.

[45] van der Heyden, F. H. J., Stein, D., Dekker, C., *Phys. Rev. Lett.* 2005, *95*, 116104.

[46] Fuentes, H. V., Woolley, A. T., *Lab. Chip.* 2007, *7*, 1524–1531.

[47] Longsworth, L. G., *J. Am. Chem. Soc.* 1953, *75*, 5705–5709.

[48] Sukas, S., De Malsche, W., Desmet, G., Gardeniers, H. J. G. E., *Anal. Chem.* 2012, *84*, 9996–10004.